Effects of cell quality in grid boundary layer on the simulated flow around a square cylinder

(Article begins on next page)

19 April 2024

Effects of cell quality in Grid Boundary Layer on the simulated flow around a square cylinder

Luca Bruno[a,*], Davide Oberto[b]

[a]*Politecnico di Torino, Department of Architecture and Design, Viale Mattioli 39, I-10125, Torino, Italy*
[b]*Politecnico di Torino, Department of Mathematical Sciences, Corso Duca degli Abruzzi 24, I-10129, Torino, Italy*

Abstract

The flow around a square cylinder is widely studied as a paradigmatic case in bluff body aerodynamics. The effects of several physical parameters of the setup, and the errors induced by turbulence models, numerical schemes and grid density have been emphasized in a huge number of studies during the past two decades. Surprisingly, the effects of the grid quality on such a class of flow has been overlooked. The lack of a shared approach and suggested best practices for high-quality grid generation among scholars and practitioners follows. The present study aims at filling this gap. The cell skewness and non-orthogonality are adopted as metrics of the grid quality. The errors induced by poor quality cells and the possible corrective measures are discussed in a Finite Volume Method framework. The effects of the cell quality on the simulated flow are systematically evaluated by a parametrical study including four different types of grid boundary layer. The obtained results are compared among them and discussed in terms of instantaneous and time averaged flow fields, stress distribution at wall, and aerodynamic coefficients. Both the overall modelling error and the skewness-induced one are evaluated with reference to a huge number of data collected from previous studies. The local error induced by few, moderately skewed, near-wall cells upwind the cylinder propagates windward because

---

*Corresponding author. Tel: + 39 011 090 4870. Fax: + 39 011 090 4999.
Email address: `luca.bruno@polito.it` (Luca Bruno)

of the convection-dominated problem, and globally affects the boundary layer separation and the vortex shedding in the wake. Skewness around the trailing edge only affects the flow to a lower extent. The skewness error on bulk aerodynamic coefficients may largely prevails on the overall modelling error, in spite of the very simple turbulence model deliberately adopted in the study. Hybrid grid boundary layer made of structured cells along the cylinder sides and unstructured ones around its edges provides results analogous to the ones obtained with a fully orthogonal grid, in spite of some clusters of few skewed cells far from the wall. Hybrid grid boundary layer is recommended as a fine balance between accuracy and flexibility in grid generation, when full orthogonal grid boundary layer is not feasible around real-world engineering applications having complicate geometries with multiple obtuse or acute edges.

---

1. Introduction

The high-Reynolds number, turbulent flow around rectangular cylinders is considered as a paradigmatic one around bluff bodies, of interest both for fundamental research and applications. In spite of the simple and nominally two-dimensional geometry, the flow is intricate, characterized by boundary layer separation, its possible reattachment depending on the ratio of the alongwind to crosswind dimensions, Kelvin-Helmholtz instability of the detached shear layer, Von-Karman-like vortex shedding along the wake. Such underlying flow regimes provide useful information on the aerodynamics of a wide range of bluff bodies of interest in civil engineering (e.g. long-span bridge decks or high-rise buildings) as well as in other engineering areas. The importance attached to such flows by the scientific community is testified by some international benchmarks, such as the ones on the flow around 1:1 square cylinder (Rodi, 2004; Rodi et al., 1997), and around 5:1 rectangular cylinder (Bruno and Salvetti, 2017; Bruno et al., 2014).

The studies within the benchmarks above have testified the high sensitivity of the flow to both physical parameters of the setup, and to errors induced by the components of the computational model. Among the former, special attention was paid for instance to the cylinder edge roundness (Tamura et al., 1998; Riberio, 2011; Cao and Tamura, 2017; Rocchio et al., 2020), Reynolds number (Scruton et al., 1971; Mannini et al., 2010; Schewe, 2013), and to other freestream conditions (e.g. Vickery, 1966; Lee, 1975; Mariotti et al., 2016; Cao and Tamura, 2018). Among the latter, the effects of turbulence models on the simulated flow have been emphasized in a huge number of studies (e.g. Franke and Rodi, 1991; Kato and Launder, 1993; Rodi, 1997; Lee, 1997; Bosch and Rodi, 1998; Sohankar et al., 2000; Ke, 2019). In their wake, the conscious and adapted application of different turbulence models is currently widespread in engineering practice. Even if to a minor extent, also the effects of the numerical schemes on the simulated flow were scrutinized by a number of studies, with special emphasis on the discretization of the convective terms (Shyy et al., 1992; Lee, 1997; Tamura et al., 1998; Cao and Tamura, 2016; Zhu et al., 2020).

More recently, the exponential growth of HPC facilities is allowing the systematic evaluation of the effects of the *grid density*, both in the vertical along-wind $x - y$ plane (Cao and Tamura, 2016) and along the spanwise z-direction (Bruno et al., 2012; Cao and Tamura, 2016; Cao et al., 2020; Zhang and Xu, 2020). The attention of other authors focused on Adaptive Mesh Refinement in Finite Element Method (see e.g. Hoffman, 2005; Berrone and Marro, 2009) and Finite Volume Method (FVM) (see e.g. Antepara et al., 2015). The errors induced by poor *grid quality* in FVM are well known in fundamental research on computational methods since the pioneering PhD Theses of Muzaferija (1994) and Jasak (1996), up to the recent studies by e.g. Ahipo and Traoré (2009); Traoré et al. (2009); Juretić and Gosman (2010); de Oliveira Samel Moraes et al. (2013); Denner and van Wachem (2014, 2015). Conversely, grid quality effects on the simulated flow around bluff bodies are surprisingly overlooked in scientific and technical literature. In particular, the current and very pervasive practice in the simulation of flow around cylinders implies that fully orthogonal

2

structured grids are generated by extrusion with constant grid spacing in the spanwise direction, but non orthogonal and skewed grids are inevitably generated in the vertical alongwind plane orthogonal to the cylinder axis. To our best knowledge, only a few number of studies partially cover such an issue. Nakane (2013) applied FVM with orthogonal and non-orthogonal grids to the low-Re (Re=550, 3000) transient flow around a circular cylinder, with focus on the early stage of the symmetrical steady reversed flow in the near wake. Haque et al. (2016) paid attention to the effects of the cell height growing ratio across the Grid Boundary Layer (GBL) on the high-Re flow around rectangular cylinders and hexagonal bridge decks. The grid quality across the GBL is expected to be of paramount importance, because of the high gradient of the velocity and turbulent variables in the boundary layer. Shortage in studies on the effects of grid quality in GBL results in the lack of a shared approach and suggested best practices among scholars and practitioners. For instance, Figure 1 provides some examples of different GBLs adopted in recent computational studies on the aerodynamics of 1:1 and 5:1 rectangular cylinders. Even if a structured
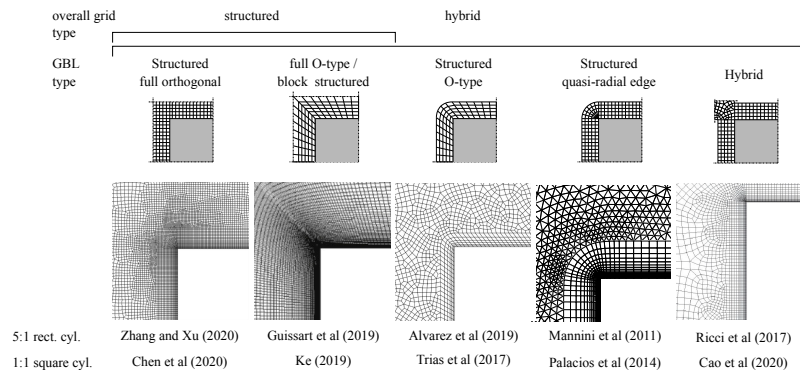

Figure 1: Types of GBL adopted in recent studies within benchmarks on the aerodynamics of 1:1 square and 5:1 rectangular cylinders

orthogonal GBL with quadrangular cells is generated in all studies along the cylinder sides, they significantly differ in the meshing strategy around the sharp

3

⁶⁵ (or slightly rounded) corners, in the shape of the cells around them, and in the
⁶⁶ grid quality in turn. A non necessary exhaustive GBL categorization is ten-
⁶⁷ tatively proposed in the figure, in the absence of a common nomenclature in
⁶⁸ literature. All meshing strategies at corners are structured, except for the 'Hy-
⁶⁹ brid GBL', where orthogonal boundary-fitted grid along the straight sides of the
⁷⁰ cylinder alternates with unstructured grid in the quadrants departing from the
⁷¹ sharp corners. The latter inevitably includes almost regular, quasi orthogonal
⁷² and skewness-free cells in the first layers around the cylinder corners because
⁷³ of the strong two-side constraint of the discretization of the adjacent edges of
⁷⁴ the structured parts. Low quality cells take place moving away from the cylin-
⁷⁵ der corners along and around the bisector of the quadrant. A single, largely
⁷⁶ prevailing GBL meshing approach among the above categories does not exist in
⁷⁷ research and engineering practice. For instance, Figure 2 provides statistics on
⁷⁸ GBLs adopted in 23 studies published in the last decade on the aerodynamics
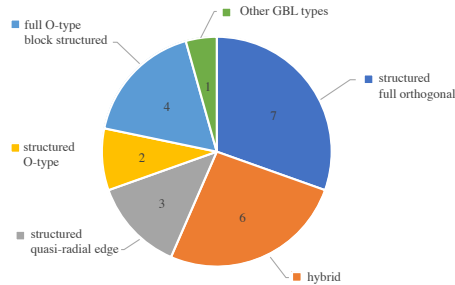of the 5:1 rectangular cylinder.

Figure 2: Statistics on types of GBL adopted in literature for the Benchmark on the Aerody-
namics of a Rectangular 5:1 Cylinder (BARC)

⁷⁹

⁸⁰ An even larger variability of GBL meshing strategies occurs for other cylinder-
⁸¹ like, real-world engineering applications having more complicate geometries with
⁸² multiple obtuse or acute edges, such as bridge deck aerodynamics. For instance,
⁸³ Tang et al. (2019) adopt a Hybrid GBL, Nieto et al. (2015) a block-structured
⁸⁴ grid, Mannini et al. (2016) a quasi radial GBL, being full orthogonal GBL un-
⁸⁵ feasible. The grid-induced errors are also expected to vary correspondingly. The

4

effects of low-quality grids could be even larger in fluid-structure interaction applications, such as bridge or cable aeroelasticity, where highly distorted cells can arise from large amplitude pitching motion of the cylinder (see e.g. Lee et al., 2016, Fig.2).

This study aims to shed some light on the errors and effects of different GBLs on the simulated flow around 1:1 square cylinder, and to compare such grid-induced errors with the modelling errors. Besides this introduction, the paper is organized into four more sections. In Section 2 the overall adopted computational model is shortly recalled, while spatial grid quality metrics and effects are detailed. The setup of the application is described in Section 3. The obtained results are commented in Section 4. Finally, in Section 5 final conclusions are drawn, and some research perspectives are briefly sketched.

2. Computational model

In the following, the adopted computational model is described in terms of turbulence model, boundary conditions, numerical approach, and spatial grid quality. Basic, well established and widely used turbulence model and numerical approach are deliberately adopted in a 2D domain. They are expected to correctly reproduce the flow of interest in qualitative terms (Lee, 1997), although with quantitative errors. Departures from top quality grid and induced errors are detailed, the study being intended to quantitatively compare the overall error model with the one induced by low-quality GBLs in the vertical alongwind plane orthogonal to the cylinder axis.

2.1. Turbulence model

The incompressible, turbulent, separated, unsteady flow around the 2D section is modeled by the classical Unsteady Reynolds Averaged Navier-Stokes (URANS) equations, which in indicial form read:

$$U_{i,i} = 0, \tag{1}$$

$$U_{i,t} + U_j U_{i,j} = -\frac{1}{\rho} P_{,i} + \left(\nu \left(U_{i,j} + U_{j,i} \right) - R_{ij} \right)_{,j}, \tag{2}$$

5

113 where U_i is the averaged velocity component in the i-th direction, P is the
114 averaged pressure, ρ the air density, and ν its kinematic viscosity, $R_{ij} = \overline{u_i u_j}$
115 the Reynolds stress, and u the velocity turbulent fluctuations. The $k - \varepsilon$ RNG
116 (Yakhot et al., 1992) turbulence model is used to close the URANS equations.
117 The Reynolds stress is expressed by the well-know Boussinesq assumption as
118 $R_{ij} = -2\nu_t S_{ij}$, where S_{ij} is the mean field strain rate, and the turbulent vis-
119 cosity ν_t is expressed as $\nu_t = C_\mu \frac{k^2}{\varepsilon}$ in terms of the turbulent kinetic energy k
120 and its dissipation rate ε. Their transport equations are

$$k_{,t} + U_j k_{,j} = -R_{ij} U_{i,j} + \left(\frac{\nu_t}{\sigma_k} k_{,i} \right)_{,i} - \varepsilon, \tag{3}$$

121

$$\varepsilon_{,t} + U_j \varepsilon_{,j} = -C_{\varepsilon_1} \frac{\varepsilon}{k} R_{ij} U_{i,j} + \left(\frac{\nu_t}{\sigma_\varepsilon} \varepsilon_{,i} \right)_{,i} - C_{\varepsilon_2}^* \frac{\varepsilon^2}{k}, \tag{4}$$

122 where $C_{\varepsilon_2}^* = C_{\varepsilon_2} + C_\mu \eta^3 \frac{(1-\eta/\eta_0)}{1+\beta\eta^3}$, and $\eta = \frac{k}{\varepsilon}\sqrt{2S_{ij}S_{ij}}$ is the ratio between the
123 turbulence time scale and the time scale of the mean field strain. The model
124 constants are $C_\mu = 0.085$, $C_{\varepsilon_1} = 1.42$, $C_{\varepsilon_2} = 1.68$, $\eta_0 = 4.38$, $\beta = 0.012$,
125 $\sigma_k = \sigma_\varepsilon = 1.393$. The cell-centered nodal values of the flow variables adjacent
126 to the wall are obtained by the standard wall function approach (Launder and
127 Spalding, 1974). Dirichlet boundary condition (b.c.) on the velocity field and
128 on the turbulent variables are imposed at the inlet. Neumann b.c. on the normal
129 component of the stress tensor, as well as the same Dirichlet b.c. on k and ε,
130 are imposed at the outlet. Periodic b.c. are imposed on both the upper-lower
131 boundaries. No-slip b.c. are imposed at the cylinder wall.

132 *2.2. Numerical approach*

133 A classic overall 2nd order approach in the framework of the Finite Volume
134 Method is adopted to discretize the governing equations above. The cell-centre
135 values of the variables are interpolated at face locations using the classic second-
136 order Central Difference Scheme (CDS) for the diffusive terms. The convection
137 terms are discretized by means of the QUICK scheme (Leonard, 1979). The
138 fully implicit second-order Euler scheme is adopted for time discretization. The
139 SIMPLE algorithm (Issa, 1986) is used for pressure-velocity coupling. The code
140 Ansys Fluent© v.18 is used.

6

2.3. Grid quality effects

142 Non-orthogonality and skewness are common issues on non-Cartesian, ar-
143 bitrary grids. A structured radial edge and an O-type GBLs are considered
in Figure 3 as examples. Both non-orthogonality and skewness are qualities
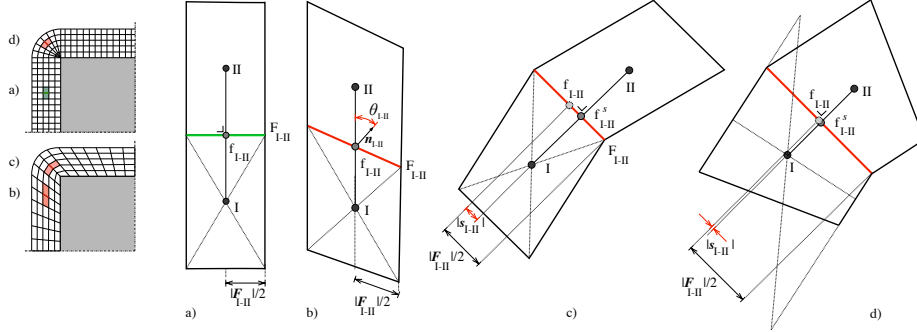

Figure 3: Face orthogonality $\theta = 0$ (a), non-orthogonality $\theta \neq 0$ (b), and skewness s (c,d) of cells around a sharp edge in different types of GBL

144

145 that refer to each face $F_{\text{I-II}}$ shared between adjacent cells with centers I and II.
146 Some pairs of cells are highlighted in Figure 3 for the sake of clarity. *Non-*
147 *orthogonality* refers to the angle $\theta_{\text{I-II}}$ between the normal vector $\boldsymbol{n}_{\text{I-II}}$ and the
148 vector connecting the two cell centers. The face is orthogonal if $\theta_{\text{I-II}} = 0$ (Fig.
149 3-a, -c, -d), non-orthogonal otherwise (Fig. 3-b). *Skewness* refers to the vector
150 $\boldsymbol{s}_{\text{I-II}}$ from the face mid-point $f_{\text{I-II}}$ to the interpolation point $f_{\text{I-II}}^s$, the latter being
151 defined as the intersection between the face and the vector connecting the two
152 cell centers. The face is not skewed if $|\boldsymbol{s}_{\text{I-II}}| = 0$ (Fig. 3-a,b), skewed otherwise
153 (Fig. 3-c,d). The examples in Figure 3 clearly underline that rectangular cells
154 are perfectly orthogonal and not skewed, and that non-orthogonality does not
155 necessarily implies skewness, and vice-versa. The above metrics can be made
156 scalar and dimensionless as $\theta_{\text{I-II}}^* = 2\theta_{\text{I-II}}/\pi$ and $s_{\text{I-II}}^* = 2|\boldsymbol{s}_{\text{I-II}}|/|\boldsymbol{F}_{\text{I-II}}|$, where
157 $|\boldsymbol{F}_{\text{I-II}}|$ is the length of the face $F_{\text{I-II}}$ (Fig. 3). Both dimensionless metrics take
158 values larger than unit for degenerate cells and interpolation points outside the
159 face, respectively.

160 Both non-orthogonality and skewness are *potential sources of errors* in the

7

numerical fluxes evaluated by FVM. *Non-orthogonality-induced error* on the diffusive terms can be pointed out by splitting the face surface vector $\boldsymbol{F}_{\text{I-II}}$ in the component $\boldsymbol{\Delta} \parallel \mathbf{d}_{\text{I-II}}$ and in a non-orthogonal one $\mathbf{k}$ (Fig. 4-a, after Jasak, 1996). Whatever the chosen direction of $\mathbf{k}$ is, the error induced on the diffusive flux of a generic variable ϕ reads in vectorial form

$$E_{no}^{d} = \nabla \cdot (\nu_{no} \nabla \phi) \tag{5}$$

where $\nu_{no} = \boldsymbol{U}_{\text{f}_{\text{I-II}}} \cdot \mathbf{k}$ is the so-called non-orthogonal viscosity, and $\boldsymbol{U}_{\text{f}_{\text{I-II}}}$ is the velocity vector at the face mid-point.

Skewness-induced error can affect the convective terms, and results in a spurious non-physical diffusion flux evaluated by Jasak (1996) as

$$E_{sk}^{c} = \nabla \cdot (\nu_{sk} \nabla \phi) \tag{6}$$

where $\nu_{sk} = \boldsymbol{U}_{\text{f}_{\text{I-II}}} \cdot \boldsymbol{s}$ is the so-called skewness viscosity. In other terms, grid skewness reduces the accuracy of interpolation to first order, and introduces a diffusion-like error in the discretized convective flux, analogously to the well-known leading truncation error of the first-order upwind scheme.

In short, both non-orthogonality and skewness indroduce non-physical diffusion, if not properly dealt. In an engineering perspective such diffusive effects are not negligible for convection-dominated, high Reynolds number flow, where physical diffusive effects play a minor role. In other terms, both grid-induced viscosities can cumulate the kinematic viscosity and the modeled turbulent one, resulting in a simulated Re number lower than the one that characterizes the actual flow.

Two approaches can be adopted to counter this problem. *High-quality grid generation* is intended to eliminate the error source, i.e. to reduce the amplitude of the geometrical metrics θ and s, and the induced errors in turn. High quality grid may be generated a priori, or obtained a posteriori by grid adaptation. Whatever the adopted technique is, such an approach is the most decisive, even if generation/adaptation criteria are required. *Corrective terms in interpolation schemes* are intended to mitigate the effects of low-quality grids, i.e. to reduce the errors (eq.s 5 and 6) without eradicate their causes.

8

188 Non-orthogonal correction strategies move from the surface vector splitting $\boldsymbol{F}_{\text{I-II}} = \boldsymbol{\Delta} + \mathbf{k}$ initially proposed by Jasak (1996) (Fig. 4-a).
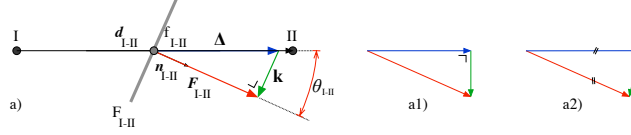

Figure 4: Approache for correction of non-orthogonality (after Jasak, 1996)

189

190 The diffusive flux for the generic variable ϕ can be approximated as

$$\boldsymbol{F}_{\text{I-II}} \cdot (\nabla\phi)_{\text{f}_{\text{I-II}}} = \boldsymbol{\Delta} \cdot (\nabla\phi)_{\text{f}_{\text{I-II}}} + \mathbf{k} \cdot (\nabla\phi)_{\text{f}_{\text{I-II}}} \approx |\boldsymbol{\Delta}| \frac{\phi_{\text{II}} - \phi_{\text{I}}}{|\mathbf{d}_{\text{I-II}}|} + \mathbf{k} \cdot (\widetilde{\nabla\phi})_{\text{f}_{\text{I-II}}}, \quad (7)$$

191 where the classic CDS is used for the orthogonal term. The non-orthogonal
192 correction second term depends on both the definition of $\mathbf{k}$, and the numer-
193 ical approximation of $(\nabla\phi)_{\text{f}_{\text{I-II}}}$. Different explicit non-orthogonal correction
194 schemes have been proposed in literature, e.g. Jasak (1996); Ahipo and Traoré
195 (2009); Traoré et al. (2009). Three possible choices for $\mathbf{k}$ are depicted in Fig-
196 ures 4(a), (a1), (a2), where the former minimizes the correction. The iterative
197 numerical approximation $(\widetilde{\nabla\phi})_{\text{f}_{\text{I-II}}}$ is generally inspired to the precursor ideas
198 in Khosla and Rubin (1974) and Muzaferija (1994). Generally speaking, the
199 non-orthogonality correction let to preserve the spatial second order accuracy.
200 However, when its contribution is larger than the orthogonal one for highly
201 non-orthogonal faces, the boundedness of the solution is no longer guaranteed
202 (Jasak, 1996). In order to ensure boundedness, the non-orthogonal correction
203 must be bounded or even discarded and the scheme becomes no longer second
204 order accurate (de Oliveira Samel Moraes et al., 2013).

205 Also skewness correction strategy is intended to correct standard interpolation
206 schemes for the quadrature values by additional term(s) accounting for $\boldsymbol{s}$. Start-
207 ing from the pioneering work of (Jasak, 1996) where the skewness problem has
208 been rigorously presented, some proposals for skewness correction have been
209 recently proposed in literature, e.g. de Oliveira Samel Moraes et al. (2013);

Denner and van Wachem (2014, 2015).

While non-orthogonal correction is widely implemented in industrial codes such as OpenFoam or Fluent, the same can not be said about the skewness correction (de Oliveira Samel Moraes et al., 2013). In the light of this, the present study aims at evaluating different strategies of GBL generation to reduce the skewness geometrical metric $|s|$, while GBL non-orthogonality is fixed according to the correction given in eq. (7).

3. Setup of the study

The adopted flow setup closely follows the one prescribed by the Ercoftac benchmark Ufr 2-02, detailed by Rodi (2004) in the QNET-CFD Knowledge Base Wiki (Rodi, 2012). The benchmark adopts as reference experimental tests the ones detailed in Lyn and Rodi (1994) and Lyn et al. (1995). The incoming flow is characterized by Reynolds number $Re = UD/\nu = 2.2e + 4$, where U is the free stream velocity and D the cylinder chord, incidence $\alpha = 0$, turbulence intensity $It = 2\%$, turbulent length scale $Lt = 0.5D$. The cylinder cross section has sharp edges and smooth surfaces. The dimensionless time step is set $\Delta t^* = 0.02tU/D$. The simulation is extended over $T \approx 300$ dimensionless time units in order to have a long enough statistical sample to secure converged statistics, after having excluded the initial transient. The dimensions of the 2D domain are given in Figure 5(a). The origin of the Cartesian coordinate is located at the center of the cylinder upwind face. The spatial grid is overall hybrid, being composed by both quadrangular and triangular cells, and by structured and unstructured partitions. A close-up view of the grid around the cylinder and its close wake is shown in Figure 5(b). In addition to usual strategies, subdomain partitioning and corresponding grid blocks are intended to ensure a dense, top-quality grid made of square cells ($\Delta_x = \Delta_y = 0.042D$) in the wake region, and to keep the grid outside the GBL unchanged for all cases.

Four types of GBLs are generated in a D-tick square annular partition around the cylinder, as detailed in Figure 5(c). All GBLs share some common

10

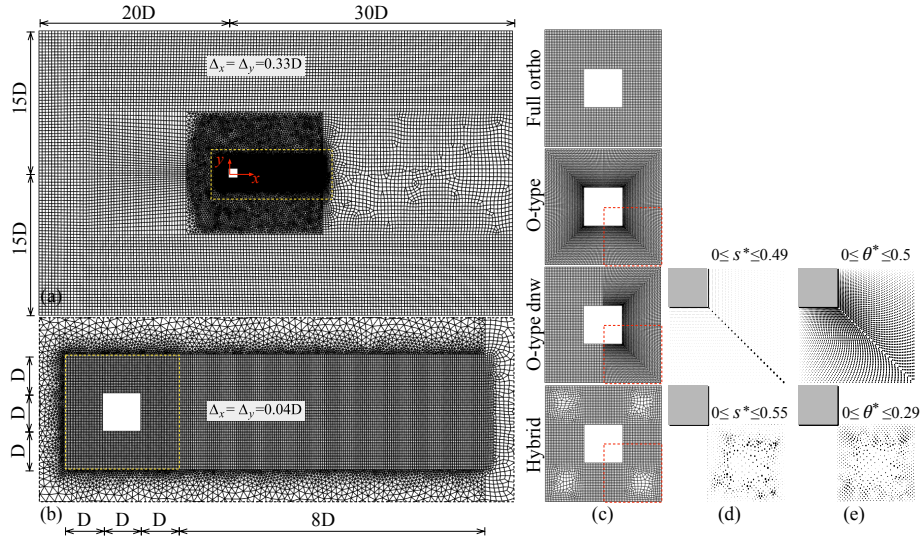Figure 5: Computational domain (a), GBL and wake subdomain (b), GBL types (c) and their dimensionless skewness (d) and non-orthogonality (e)

features, in order to allow a proper comparative parametric study: cylinder side uniformly discretized; height of the first cell at wall equal to $\Delta n/D = 1/24$; growing ratio equal to unit (nil grid gradient) and number of cells equal to 24 across the structured parts of the GBL. Δn is set to comply the requirements of wall-function-based near-wall treatment about the height of the control volumes at wall: the wall unit $n^+ = nu_*/\nu$ results in the range $25 \leq n^+ \leq 55$. The generated GBLs share the discretization of the quadrant edges, but differ in the type of grid. The 'Full ortho' GBL has the same top quality grid a in the wake. The 'O-type' one is characterized by a block-structured non-orthogonal grid. The 'O-type dnw' GBL is a mix of the previous ones, where O-type grid is limited to the downwind half of the annular partition. In contrast to the previous GBLs, a 'Hybrid' GBL is not uniquely defined by the discretization of the outer edges of the quadrants, but it necessarily depends also on the specific algorithm adopted for grid generation. In the present study, a paving, advancing-front-based algorithm is employed (Blacker and Stephenson, 1991). The resulting,

11

specific realization of the Hybrid GBL shows the general distinctive features of this class of GBLs as detailed in the introduction. However, in this specific case the density and quality of the cells do not monotonically decrease moving away from the wall as usually (see e.g. Fig. 1), because of nil grid gradient across the structured parts of the GBL. Skewness and non-orthogonality are nil everywhere in the GBL for the 'Full ortho' GBL and the upwind part of the 'O-type dnw' one. The spatial patterns of dimensionless skewness and non-orthogonal metrics are given by scatterplots in Figures 5(d) and (e), respectively, for the other cases and limited to the quadrant enclosed by the red dashed line. The s^* pattern in O-type GBLs groups skewness $s^* \neq 0$ along the diagonal only, while $\theta^* \neq 0$ is distributed in the rest of the field. Significant values of both s^* and θ^* are more scattered in the generated Hybrid GBL, with the highest values in correspondence of the transition between dense and coarse grid. In particular, the present Hybrid GBL shows nearly nil skewness in the first 3 cell rows around the cylinder corners (corresponding to a width of $1/8D$), because of the constraints imposed by the adjacent edges of the structured parts on the adopted mesh generation algorithm. It follows that the Hybrid GBL is locally quite similar to the Full ortho GBL in such a region.

A quantitative statistical description of the patterns above is given in Table 1. Overall, two main comments follow. First, the maximum values of both metrics are comparable among GBLs, and moderate ($\max(\phi) \lesssim 0.5$). In other terms, cells in GBLs are moderately skewed (the intersection point is no longer distant than $|\boldsymbol{F}_{\text{I-II}}|/4$ from the face mid-point) and moderately non-orthogonal ($\theta \leq 45°$). Second, s^* and θ^* values significantly greater than zero ($\phi \geq 0.1$) rarely occur, except for θ^* in O-type GBL. In other terms, GBL are very locally skewed only. In follows that average and median values are very low, in turn. Bearing in mind that non-orthogonality errors will be numerically corrected, it might be inferred that all GBLs have comparable overall good quality, while point-wise moderately-skewed cells are source of errors only.

12

Table 1: Statistics on dimensionless skewness and non-orthogonality for different GBL types

ϕ	GBL	$\max(\phi)$	$\%_f\,\|\,\phi > 0.1$	$\mathrm{avg}(\phi)$	$\mathrm{median}(\phi)$	discrete distributions
θ^*	Hybrid	0.2857	7.2%	0.0223	0	
	O-type	0.4955	83.9%	0.2778	0.2952	
s^*	Hybrid	0.5532	8.5%	0.0241	1e-6	
	O-type	0.4884	0.7%	0.0061	0.0047	

4. Results

The present results are compared and discussed among them, in order to evaluate the errors induced by skewed cells in different regions of the GBL (Hybrid, O-type and O-type dnw grids) with respect to the full orthogonal grid (Full ortho). Furthermore, the present results are compared with a huge, even if not necessarily exhaustive, number of published studies on the same flow around square cylinder at Re=22,000, in the wake of the Ercoftac QNET-CFD Knowledge Base Wiki benchmark (Rodi, 2004, 2012). The goal of such a comparison is twofold: first, assessing the overall modelling error of the GBL-error-free simulation (Full ortho) with respect to the most accurate results in literature, and to compare it with the skewness-induced errors; second, placing the present results in the perspective of the whole scientific production on the topic, with special interest to the variability of the results obtained with different approaches. Both experimental tests spanning about 50 years (Pocha, 1971; Wilkinson, 1974; Lee, 1975; Otsuki et al., 1978; Bearman and Obasaju, 1982; Durao et al., 1988; Sakamoto et al., 1989; Lyn and Rodi, 1994; Lyn et al., 1995; Nishimura, 2001; Noda and Nakayama, 2003; Liu et al., 2015; Moore et al., 2019, in chronological order), and computational studies are considered. Among the latter, different approaches to turbulence modelling are considered: from the

13

pioneering so-called No-Model Simulations (NMS, Tamura and Ito, 1996) and LES (Murakami and Mochida, 1995; Yu and Kareem, 1996), to URANS (Franke and Rodi, 1991; Kato and Launder, 1993; Deng et al., 1994; Wang and Vanka, 1997; Bosch and Rodi, 1998; Shimada and Ishihara, 2002; Younis and Przulj, 2005) and hybrid models (Ke, 2019), up to LES (Sohankar et al., 2000; Oka and Ishihara, 2009; Cao and Tamura, 2016; Chen et al., 2020), recent NMS (Cao et al., 2020), and DNS (Trias et al., 2015).

For the sake of clarity, in the following the obtained results are schematically arranged in three subsections. The simulated flow field around the cylinder is discussed first, the distributions of the stresses at wall are commented in the second section, while the bulk force coefficients are compared in the last one.

4.1. Flow field

In order to provide an overall sound phenomenological picture of the simulated flow topology, the instantaneous flow patterns around the cylinder and in its wake are plotted in Figure 6. All the flow patterns refer to the same vortex-shedding phase, corresponding to the local maxima of the lift force. For the sake of brevity, the isocontours of the vorticity magnitude $|\omega_z|$ from two grids are included only, corresponding to the highest (Full ortho, Fig. 6-d) and lowest (O-type, Fig. 6-e) grid quality. The present results are compared between them and with analogous flow visualizations from past studies: DNS by Trias et al. (2015) (background color according to the magnitude of the pressure gradient); NMS by Cao et al. (2020) (densest z-wise grid, background color according to the streamwise velocity component); 2D URANS simulation by Shimada and Ishihara (2002) (isocontours of the vorticity magnitude). Visualizations are sorted by expected decreasing overall accuracy of the computational model. In spite of their different state variables and contour values, qualitative and quantitative remarks can be drawn. The von Kármán-like vortex street clearly emerges in the wake in every simulation. However, the simulated vortex pattern exhibits significant differences. A common trend can be recognized in visualizations from a) to d): the lower the expected overall model accuracy, the
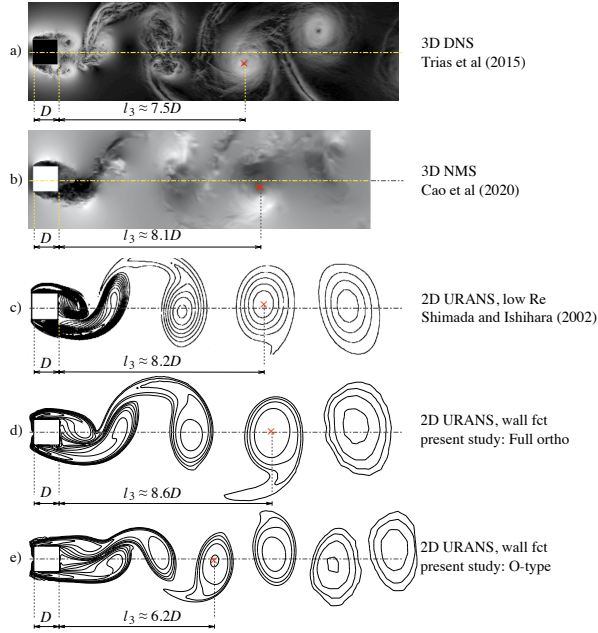
14

Figure 6: Instantaneous flow fields along the wake at the same vortex-shedding phase ($t = argmax(C_L)$) simulated by different computational models

slightly longer the longitudinal spacing between successive vortices. Conversely, this trend is no longer monotonic moving from the Full ortho (d) to the skewed O-type GBL (e): the vortex spacing drastically shortens. The distance l_3 between the trailing edge and the centre of the 3rd vortex in the wake is estimated by hand-picking to quantitatively support such a qualitative trend. Correspondingly, the wake width simulated by skewed O-type GBL (e) is clearly narrower than in Full ortho GBL (d). The wake features above appear correlated to the curvature of the shear layer along the side surface just downwind the separation point at the leading edge, and to the vortex shedding close to the trailing edge, in turn. Simulations (a)-(d) are qualitatively consistent in predicting a highly curved shear layer, and shedding point close to the rear face. Conversely, skewed O-type GBL returns a lower curvature of the shear layer, and a shedding point further away in the wake.

15

345 Figure 7 shows the time averaged vorticity $t - avg(\omega_z)$ field around the cylinder base surface. The experimental PIV-based visualization by Moore et al.
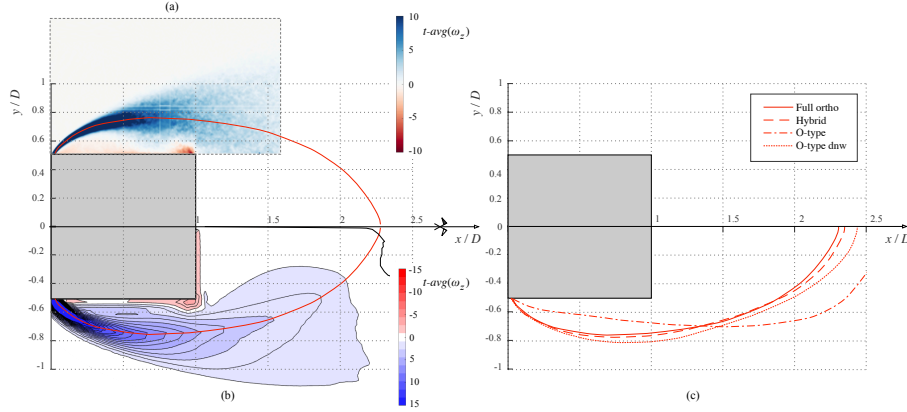

Figure 7: Mean flow field around the cylinder: time averaged vorticity $t - avg(\omega_z)$ measured by Moore et al. (2019) (a), and simulated by the full orthogonal GBL (b); shape of the shear layer by loci of $max(t - avg(\omega_z))$ simulated by different GBLs (c)

346

347 (2019) is given in Figure 7(a), while the corresponding field simulated by the Full 348 ortho GBL is plotted in Figure 7(b). Both fields refer to the lower side surface, 349 the experimental field being mirrored along the x axis to facilitate comparison. 350 The red curve in both subfigures is the locus of maxima $max(t - avg(\omega_z))$ sim-351 ulated by Full ortho GBL, i.e. it visualizes the shape of the simulated shear 352 layer. The Full ortho simulation is in excellent qualitatively agreement with 353 the experiment, in spite of the relatively simple overall computational model. 354 The red curve closely follows the axis of the experimental blue plume, i.e. the 355 separated shear layer. Finally, the Full ortho GBL simulates the negative time-356 averaged vorticity induced by the secondary clockwise vortex at the trailing 357 edge, in qualitative agreement with PIV measurements. Figure 7(c) collects 358 the loci of $max(t - avg(\omega_z))$ for the four different GBLs. It can be observed 359 that: i. the shapes of the shear layer obtained by the Full ortho and the Hybrid 360 GBLs are very close in spite of the scatted skewness shown by the latter; ii. 361 the O-type dnw curve slightly differs from the previous two, especially in the

16

³⁶² wake; iii. the O-type curve completely departs from the others. On the one
³⁶³ hand, such findings quantitatively confirm in time average what discussed in
³⁶⁴ qualitative terms about the instantaneous patterns (Fig. 6-d, -e). On the other
³⁶⁵ hand, they suggest that very local skewness-induced errors along the diagonals
³⁶⁶ of the square annular partition globally affect the whole separated flow.   The
³⁶⁷ closer the error source to the separation point at the cylinder edge, the more
³⁶⁸ significant its global effects (see e.g. the O-type GBL in Fig. 5-d). Conversely,
³⁶⁹ a local high quality of the cell closely around the separation point preserves the
³⁷⁰ accuracy of the results in spite of high skewness elsewhere (see e.g. the Hybrid
³⁷¹ GBL in Fig. 5-d). Such errors are introduced along the diagonals of the square
³⁷² annular partition, and in particular close to the separation point at the cylinder
³⁷³ edge in the O-type GBL.

³⁷⁴   In order to check such a conjecture, Figure 8 relates the skewness viscos-
ity to other simulated flow variables in the lower near wall region. The time
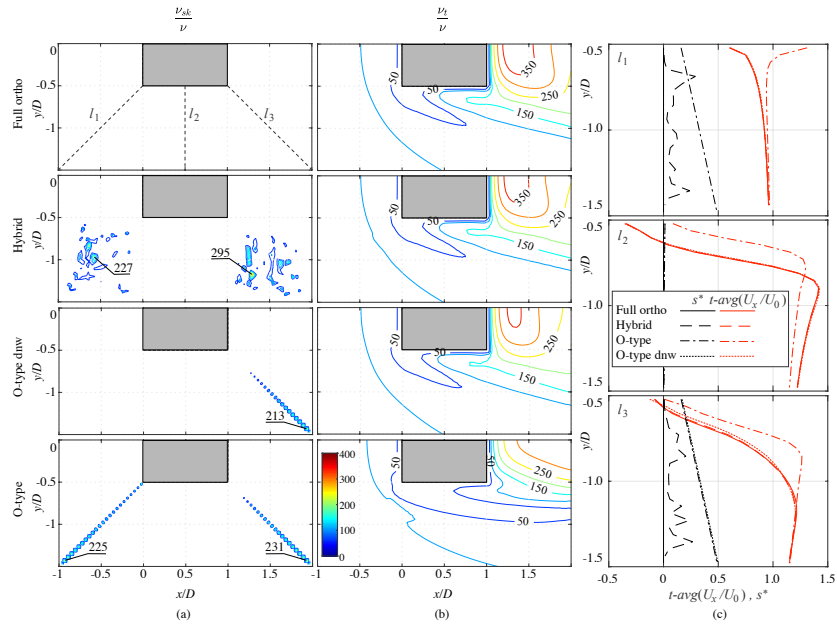
Figure 8: Time-averaged skewness viscosity ratio (a), turbulent viscosity ratio (b), $x-$velocity
(red lines) and skewness (black lines) profiles (c)

³⁷⁵

17

averaged skewness viscosity (ν_{sk}, Eq. 6, Fig. 8-a) are compared to the time averaged turbulence eddy viscosity of the URANS model (ν_t, Eq.s 3-4, Fig. 8-b). Both quantities are normalized with respect to the kinematic viscosity ν. Two main remarks follow. First, ν_{sk} is not distributed all over the domain but only where skewed faces are located (Fig. 5-d). Second, ν_{sk} and ν_t take on values within the same order of magnitude, hundreds of time larger than the kinematic viscosity: in other term, false skewness viscosity potentially affects the solution to the same extent of the turbulence model. In particular, ν_{sk} has a dramatic relative importance upwind the leading edge, where transition to turbulence not yet occurs, and ν_t is very low. Three different 1D domains l_1, l_2, l_3 are defined, as sketched in Figure 8(a), first row. Figure 8(c) shows the profiles of the dimensionless skewness and time-averaged horizontal velocity U_x along such lines. Three main remarks follow. First, skewed faces lie along l_1 in both Hybrid and O-type GBL. However, only the O-type U_x profile departs from the others and shows a non-physical flow acceleration very close to the wall. We can infer that skewness viscosity plays a dramatic detrimental role mainly close to the wall, approximately in the first 2 / 4 cell rows (see Fig. 5-d). Second, an analogous scatter between O-type GBL and the other simulations is observed along l_2, even if the cells are locally unskewed and orthogonal in all GBLs. It means that the *local skewness error* introduced by O-type GBL along l_1 is *transported by convection* along the side surface, analogously to the modeled state variables. From a physical point of view, this implies *global effects*: the reversed flow predicted by Full ortho, Hybrid and O-type dnw GBLs is not adequately grasped by the O-type GBL. Finally, the very small scatter between the U_x profiles by Full ortho and O-type dnw GBLs along l_3 testifies that the skewness viscosity, its error and its effects not depend only on $s*$, but on the velocity field, too (Eq. 6).

In order to quantitatively compare the present results with the ones in literature, the distributions of the dimensionless streamwise velocity U_x/U_0 averaged in time ($t-avg$ in the following) and in the spanwise direction ($z-avg$ in the following, relevant to 3D models) are plotted in Figure 9(a) along the wake

centerline $y = 0$. In particular, available experimental measurements (Durao
et al., 1988; Lyn and Rodi, 1994), high-fidelity DNS (Trias et al., 2015) and
LES (Cao and Tamura, 2016), and other LES and URANS results are consid-
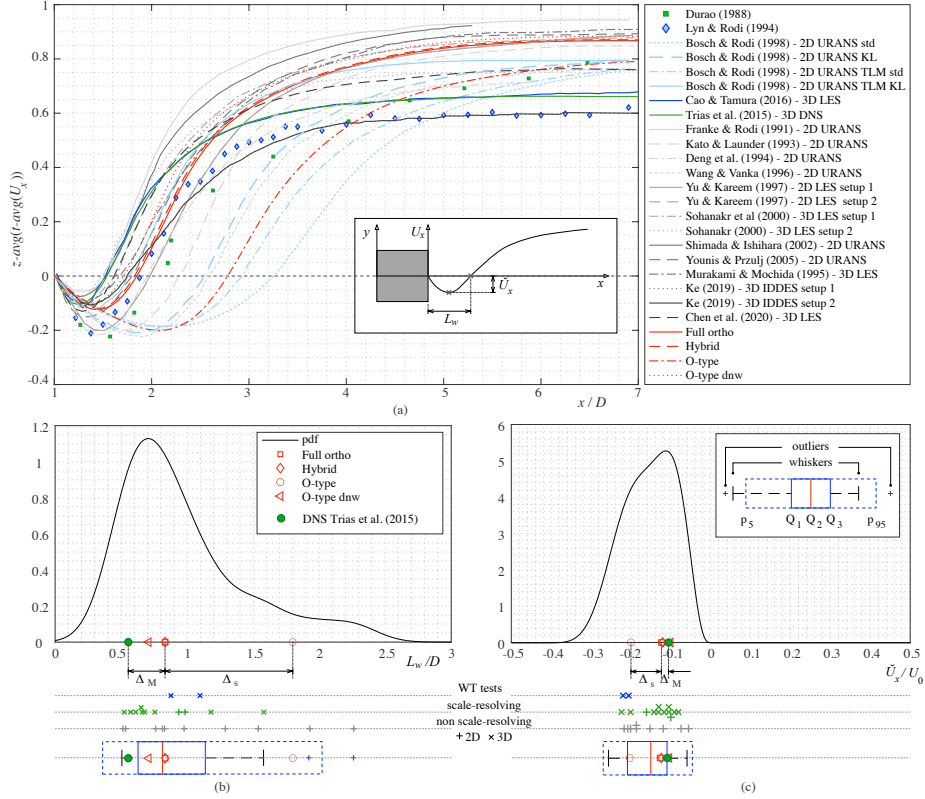ered.   In general, the considered high-fidelity simulations provide consistent

Figure 9: Distribution of time-averaged $x-$velocity along $y = 0$ (a), statistics of the wake recirculation length L_w (b) and velocity defect $\breve{U}_x$ (c)

410

results. However, as pointed out by the same Trias et al. (2015), their computa-
tional results slightly but systematically differ from the reference experimental
data of Lyn and Rodi (1994), with remarkable differences in the near wake re-
circulation region, where the simulated reversed velocity is nearly half of the
measured one. The Lyn and Rodi (1994) measurements significantly depart in
turn from the previous measures by Durao et al. (1988), and even larger variabil-

19

₄₁₇ ity takes place among other computational results, even if the same approach to
₄₁₈ turbulence modelling is adopted. Such overall variability of the velocity profiles
₄₁₉ results in scattered values of the recirculation length, of the maximum reversed
₄₂₀ speed, and of the velocity plateau along the fare wake, if any. In particular,
₄₂₁ the streamwise velocity profiles predicted by low-skewness grids (Full ortho and
₄₂₂ Hybrid) are in satisfactory agreement with experimental data in the near wake,
₄₂₃ while the velocity recovery is overestimated in the far wake $x/D > 2.5$. The
₄₂₄ dense and orthogonal grid in the wake (Fig. 5), and the 3rd order scheme used
₄₂₅ for the convective terms suggest that most of the underlying error can be tenta-
₄₂₆ tively ascribed to the 2D domain, and/or to adopted turbulence model, namely
₄₂₇ to the empirical modelling of $C^*_{\varepsilon_2}$. The velocity distribution issued from O-type
₄₂₈ grid dramatically suffers the effects of the skewness viscosity (eq. 6), resulting
₄₂₉ in the striking overestimation of the recirculation length. Conversely, skewness
₄₃₀ around the trailing edge only (O-type dnw) has the opposite effects of the skew-
₄₃₁ ness around both leading and trailing edges (O-type), i.e. it shortens the recircu-
₄₃₂ lation length and reduces the velocity defect with respect to the Full ortho grid.
₄₃₃ Two local metrics are retained in order to synthetically describe the near wake
₄₃₄ recirculation region: the wake recirculation length L_w, and the velocity defect
₄₃₅ $\breve{U}_x$, graphically defined in Figure 9(a) for the sake of clarity and conciseness. In
₄₃₆ the light of the high variability highlighted above, statistics are obtained on each
₄₃₇ of them, by referring to the ensemble of realizations collected in literature and
₄₃₈ plotted in Figure 9(a). Statistics are visualized in Figures 9(b) and (c) for L_w/D
₄₃₉ and $\breve{U}_x/U_0$, respectively. All realizations are reported and categorised in Wind
₄₄₀ Tunnel (WT) measurements, non scale-resolving (RANS/URANS), and scale-
₄₄₁ resolving (DNS, NMS, LES, DES, IDDES) simulations. The *a-priori* expected
₄₄₂ highest-fidelity model (DNS, Trias et al., 2015) is pointed out. Non paramet-
₄₄₃ rical Probability Density Functions (PDF) with positive and negative support
₄₄₄ are fitted on the whole ensemble for L_w and $\breve{U}_x$, respectively, and accompanied
₄₄₅ by the corresponding box plots. Such a postprocessing allows a twofold reading
₄₄₆ of the obtained results. In a deterministic reading, the present overall mod-
₄₄₇ elling error Δ_M is evaluated by the scatter between the highest-fidelity model

20

(DNS, Trias et al., 2015) and the present highest-quality GBL (Full ortho), while the highest skewness-induced error Δ_s is given by the scatter between the highest (Full ortho) and lowest (O-type) GBL quality. In a purely statistical reading, each realization can be associated with the corresponding percentile, i.e. the number where a certain percentage of scores fall below it. Here, we are aware that the ensemble cardinality ($\#=22$) is significant but not necessarily high enough to ensure full statistical convergence. Hence, we prefer a coarse statistical mapping of the present results by referring to outliers, and to the intervals between percentiles p_5, $p_{25} = Q_1$, $p_{50} = Q_2$, $p_{75} = Q_3$, p_{95}. Selected remarks follow from both perspectives: i. for both metrics the skewness-induced error is by far larger than the overall modelling error, despite the latter results form top- (3D DNS) and low- (2D URANS) ranked models; ii. L_w/D shows a variability (coefficient of variation $c.o.v.(L_w) = \sigma(L_w)/|\mu(L_w)| = 0.236$) lower than $\breve{U}_x/U_0$ ($c.o.v.(\breve{U}_x) = 0.364$); iii. the values provided by the Full ortho and Hybrid grids are within the $[Q_1 Q3]$ range for both metrics, while the L_w/D value from O-type grid is clearly an outlier, and the corresponding $\breve{U}_x/U_0$ is close to Q_1.

4.2. Stress distributions at wall

The distributions of the dimensionless wall shear stress τ_w averaged in time and in the spanwise direction are plotted in Figure 10 versus the curvilinear axis s along the upper half perimeter. Positive values correspond to τ_w with the same direction of the curvilinear axis. The distributions obtained by different GBLs are compared with the ones obtained by Cao and Tamura (2016) with different grid densities. A closed view along the side surface is given, in analogy to what done by Cao and Tamura (2016) as well. The distributions by this study follows from a wall-function modelling approach and, consequently, the size of the cells along the wall is much larger than the ones in Cao and Tamura (2016) in both s and n directions. The s-wise low grid density implies a scarce resolution of the wall shear stress profile, testified by the coarse placement of the peaks immediately upstream and downstream the leading corner B.

21

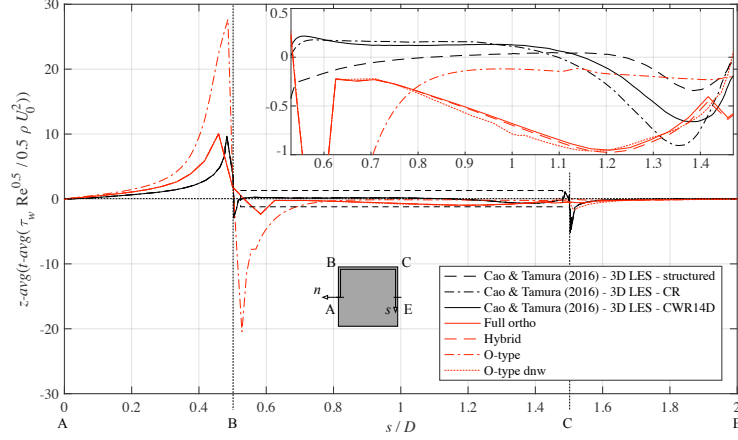Figure 10: Distribution of time-averaged dimensionless wall shear stress along the upper half perimeter

478 However, the maxima of $|\tau_w \mathrm{Re}^{0.5}/0.5\rho U_0^2| \approx 10$ and 2.5 predicted by Full ortho,

479 Hybrid and O-type dnw GBLs well matches the LES results in Cao and Tamura

480 (2016). Both s and n-wise low grid density does not allows the simulation of the

481 small-size counterclockwise secondary vortices downstream B ($0.5 < s/D \lesssim 0.7$)

482 and upstream the trailing corner C ($1.47 \lesssim s/D < 1.5$) visualized in Cao and

483 Tamura (2016)-Fig. 10, and Cao et al. (2020)-Fig. 10. This yields to reversed

484 flow all along the side surface, and corresponding negative τ_w. The "3D LES-

485 structured" simulation by Cao and Tamura (2016) is affected by an analogous

486 issue. The O-type distribution drastically differs from the others because of both

487 local and global effects of the skewness viscosity. The local peaks around B are,

488 in absolute value, from 3 to 8 times higher than the ones issued by the other

489 GBLs. After a shear recovery, the distribution attains a plateau value close to

490 zero along the downwind half of the side surface, i.e. the flow is unrealistically

491 quasi-stagnant. Conversely, the effects of the skewness viscosity on τ_w induced

492 by O-type dnw GBL mainly take place around the trailing corner only, because

493 of the convection-dominated flow.

494 The distributions of the time-averaged and time-standard deviation ($t - std$

22

in the following) of the pressure coefficient Cp, also averaged spanwise and between the upper and lower half perimeters ($side - avg$ in the following) are plotted in Figure 11 (a) and (b), respectively. They are compared to available experimental measurements, high-fidelity DNS (Trias et al., 2015) and LES (Cao and Tamura, 2016), and several other LES and URANS simulations. In spite of the same nominal setup, both experimental and computational results are significantly scattered along the whole base surface, especially in regard to $t - std(Cp)$. Interestingly, distribution from *a-priori* high-fidelity simulations are extremal occurrences at the lower and upper bounds of the ensemble for $t - avg(Cp)$ and $t - std(Cp)$, respectively. Conversely, Full ortho GBL distributions lie around the upper and lower bounds of the ensemble for $t - avg(Cp)$ and $t - std(Cp)$, respectively. In short, the adopted computational model slightly underestimates the mean suction and the pressure fluctuations, and notably fails in predicting the local maximum of $t - std(Cp)$ in the downwind half of the side surface. Hybrid GBL provides the same mean distribution, and negligible differences take place for the pressure standard deviation. O-type dnw GBL does not significantly affect the mean distribution, while the local error made at the trailing edge C makes the $t - std(Cp)$ distribution closer to the average of the experimental measurements. We conjecture that such a misleading agreement is induced by a deeper footprint of the vortex shedding on the side surface, induced by small changes in the flow structure in the near wake. Highly skewed O-type GBL dramatically and qualitatively affects both the distributions of the Cp mean and standard deviation. Their trend is typical of a streamlined body rather than of a bluff body: deep mean suction occurs at the leading edge B; mean pressure plateau is missing downstream it, and mean pressure recovery takes place along the side surface; pressure standard deviation is one order of magnitude lower than the average of the results in literature.

Analogously to what done for the streamwise velocity in the wake, four s-wise averaged metrics are defined to synthetically describe the time-averaged and time-fluctuating pressure field along the side ($l - avg$) and rear ($b - avg$) surfaces. The bounds of the averaging lengths $l1$, $l2$, b are intended to discard
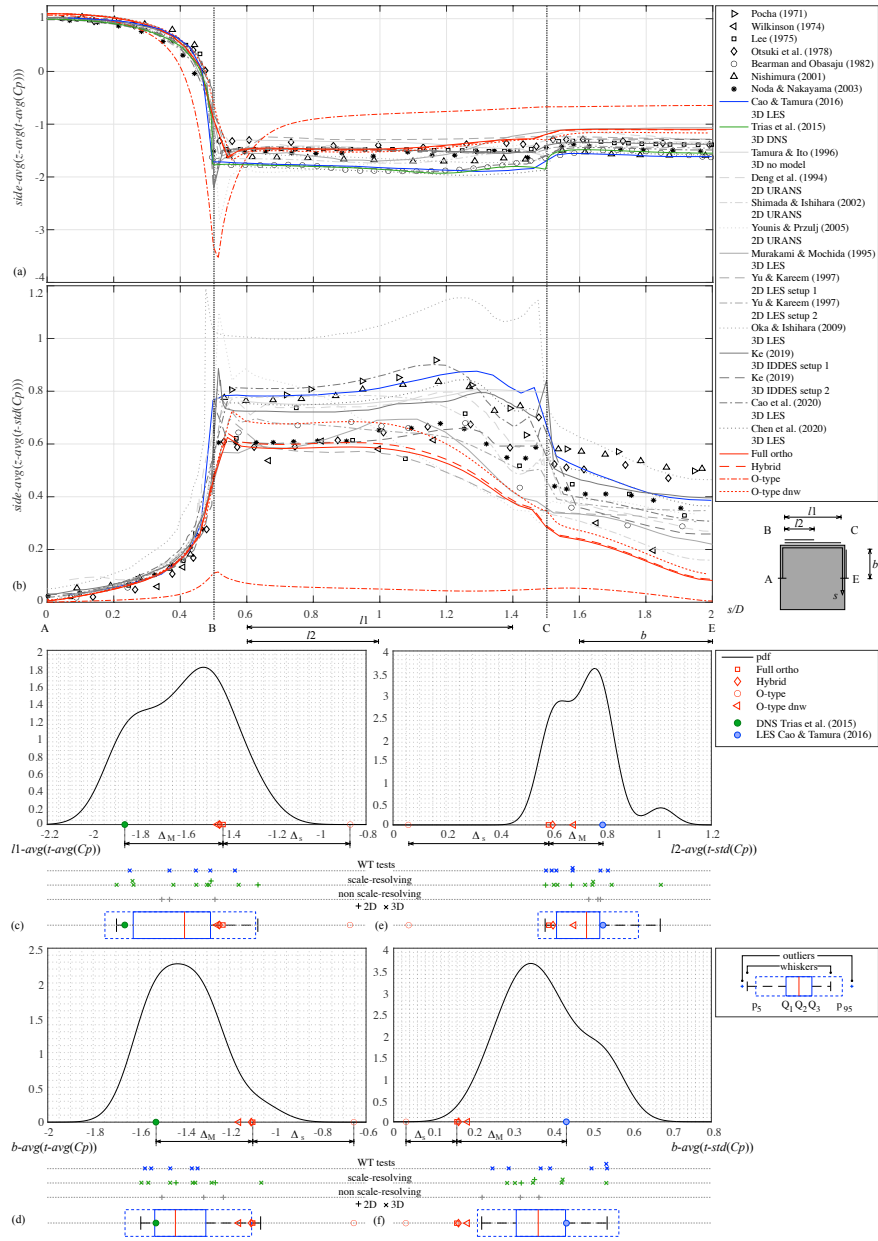
23

Figure 11: Cp distribution: time-averaged value (a), time-standard deviation (b), statistics of the side (c,e) and base (d,f) pressure

⁵²⁶ the neighbourhood of the sharp edges, and related local high pressure gradients.

⁵²⁷ The cardinality of the ensemble of the realizations ($\#$=21) is close to the one

⁵²⁸ used for the streamwise velocity in the wake. The 3D LES by Cao and Tamura

⁵²⁹ (2016) is chosen as *a-priori* highest-fidelity model when DNS results from Trias

⁵³⁰ et al. (2015) are not publicly available. Figures 11(c) and (d) show the distribu-

⁵³¹ tions of the side and rear surface $t - avg(Cp)$ plateaux. The following remarks

⁵³² can be drawn: i. the coefficients of variation of the literature results are similar

⁵³³ $(c.o.v.(l1 - avg(t - avg(Cp))) = 0.12$, $c.o.v.(b - avg(t - avg(Cp))) = 0.1)$ and

⁵³⁴ not negligible; ii. in a statistical setting, the Full ortho, Hybrid and O-type

⁵³⁵ dnw realizations are close to Q_3 of $l1 - avg(t - avg(Cp))$ and to and p_{95} of

⁵³⁶ $b - avg(t - avg(Cp))$, while the O-type ones are outliers in both cases; iii. in a

⁵³⁷ deterministic setting, the skewness errors Δ_s are comparable to the model ones

⁵³⁸ Δ_M. Figures 11(e) and (f) show the distributions of $t - std(Cp)$ over $l2$ and b,

⁵³⁹ respectively. The following remarks can be drawn: i. the c.o.v. of the distribu-

⁵⁴⁰ tions of the Cp standard deviation in literature are overall higher than the ones

⁵⁴¹ of the time-averaged pressure. In particular, the c.o.v. of the pressure standard

⁵⁴² deviation along the rear face $(c.o.v.(b - avg(t - std(Cp))) = 0.25$, Fig. 11-f) is

⁵⁴³ higher than the one on the side surface $(c.o.v.(l2 - avg(t - std(Cp))) = 0.15$, Fig.

⁵⁴⁴ 11-e), and impressive in absolute terms. The slight bi-modality of the PDF in

⁵⁴⁵ Figure 11(e) does not seem to depend on the approach/model used; ii. over the

⁵⁴⁶ $l2$ domain, while the Full ortho and Hybrid realizations are located near Q_1 and

⁵⁴⁷ the O-type dnw one in between Q_1 and Q_2, the O-type realization is an outlier;

⁵⁴⁸ iii. over the domain b, all the realizations of the present work are outliers even if

⁵⁴⁹ Full ortho, Hybrid and O-type dnw are close to p_5; iv. the deterministic model

⁵⁵⁰ error Δ_M is prevailing over the skewness one Δ_s along b only, while the opposite

⁵⁵¹ is the case along $l2$.

4.3. Bulk forces

⁵⁵³ Bulk force coefficients are scarcely useful in shedding light on phenomenolog-

⁵⁵⁴ ical local features of the simulated flows and skewness effects on them. Neverthe-

⁵⁵⁵ less, they are of great importance for design purposes in engineering applications.

The main bulk force coefficients obtained in the present study are compared and discussed with reference to statistics on the same metrics obtained in different wind tunnel and computational studies in Figure 12: $t - avg(C_D)$ is the time- and spanwise-averaged drag coefficient per unit length; $t - std(C_L)$ is the standard deviation of the time variation of the lift coefficient; $St = f_s D/U_0$ is the Strouhal number, where the shedding frequency f_s is evaluated from the time fluctuations of the lift coefficient. Statistics are obtained from ensembles having a cardinality equal to #=39 for $t - avg(C_D)$ and St, and #=29 for $t - std(C_L)$. Realizations are collected from Liu et al. (2015), Trias et al. (2015), Cao and Tamura (2016), and references therein. PDFs of $t - avg(C_D)$ and $t - std(C_L)$
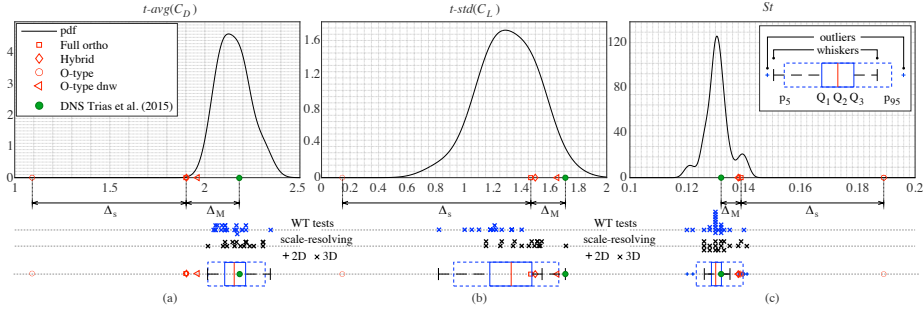
Figure 12: Bulk parameters: statistics of time-averaged drag coefficient (a), standard deviation of the lift coefficient (b), Strouhal number (c)

are moderately skewed and unimodal. The three-mode PDF of the St number seems not due to the selected approach: for instance, WT realizations contribute to all modes. The coefficient of variation is small for the time-averaged drag $(c.o.v.(t - avg(C_D)) = 0.04)$ and Strouhal number $(c.o.v.(St) = 0.03)$, while it is significant for lift fluctuations $(c.o.v.(t - std(C_L)) = 0.15)$. The *a priori* high fidelity model closely fits the ensemble average value of $t - avg(C_D)$ and St. Conversely, DNS significantly overestimates the $t - std(C_L)$ in respect to the whole ensemble, and to the experimental measurements in particular. We conjecture this can be ascribed to the unsatisfactory simulation of the spanwise pressure correlation, probably due to too short spanwise domain size, and/or to

26

₅₇₆ poor grid density in the same direction (Bruno et al., 2012). Both modelling and
₅₇₇ skewness errors imply the reduction of $t - avg(C_D)$ and $t - std(C_L)$, while the
₅₇₈ Strouhal number increases under the effects of both Δ_M and Δ_S. The skewness
₅₇₉ error is much higher than the modelling one for all bulk metrics: 2.9 times for
₅₈₀ $t - avg(C_D)$, 5.4 times for $t - std(C_L)$, 7.2 times for St. Let us consider the
₅₈₁ drag coefficient as an example (Fig. 12-a). The ensemble median is $Q_2 \approx 2.15$,
₅₈₂ and DNS returns a reference value $t - avg(C_D)_{rep} \approx 2.18$ (71-th percentile in in
₅₈₃ probabilistic terms), while Full ortho and Hybrid GBL predict $t - avg(C_D) \approx 1.9$
₅₈₄ (corresponding to the 0.01-th percentile, and resulting in $\Delta_M \approx 0.28$), and O-
₅₈₅ type GBL $t - avg(C_D) \approx 1.1$ (corresponding to a full outlier, and resulting in
₅₈₆ $\Delta_s \approx 1.08$). It follows that both modelling and skewness errors lead to the
₅₈₇ unsafe estimation of the drag force. However, the design could be effectively
₅₈₈ secured versus Δ_M by adopting a partial safety factor γ_Q for variable actions,
₅₈₉ also accounting for model errors/uncertainties (e.g. $\gamma_Q = 1.5$ in EN 1990, 2002;
₅₉₀ EN 1991-1-4, 2005, for wind action in structural engineering). The same usual
₅₉₁ value of the partial safety factor is not effective face to the large skewness error.
₅₉₂ Analogous comments are relevant to $t - std(C_L)$ and St, if the deviation of the
₅₉₃ Strouhal number has unfavourable effects on the structural response.

₅₉₄ 5. Conclusions

₅₉₅ The flow around a square cylinder at Re=22,000 is simulated under four
₅₉₆ types of Grid Boundary Layers, the other components of the computational
₅₉₇ model being unchanged. GBLs differ in cell quality, while they share common
₅₉₈ other features, such as the geometry of their boundaries, their size, the grid den-
₅₉₉ sity at wall, the grid in the outer part of the computational domain. Thanks to
₆₀₀ this, the effects of the cell skewness are separately discussed with respect to the
₆₀₁ ideal full orthogonal GBL. The attention paid in the recent past to the adopted
₆₀₂ benchmark by the scientific community allowed a huge number of previous re-
₆₀₃ sults to be collected and statistically analyzed. Hence, the obtained results are
₆₀₄ compared not only among them, but also with such a huge database.

Some conclusions can be summarized:

- The local error induced by few, moderately skewed, near-wall cells upwind the cylinder propagates windward because of the convection-dominated problem. The error globally and significantly affects the boundary layer separation and the vortex shedding in the wake. The same skewed cells around the trailing edge only affect the flow to a lower extent;

- The skewness error on bulk aerodynamic coefficients may largely prevails on the overall modelling error, despite a very simple turbulence model and a second-order accurate numerical approach are deliberately adopted in the study;

- O-type, block structured, skewed GBL results in the qualitative simulation of the instantaneous vortex street in the wake, and in the concurrent dramatic underestimation of the lift fluctuating component by a factor 5. Such results call to mind the well renowned quote by Ferziger (1993): *"The greatest disaster one can encounter in computation is not instability or lack of convergence, but results that are simultaneously good enough to be believable, but bad enough to cause trouble"*;

- Hybrid GBL with unstructured patterns around the cylinder edges can provide results analogous to the ones obtained with a full orthogonal grid, provided that from 2 to 4 cell rows nearly orthogonal and skewness-free are generated near the wall (corresponding to a width from $1/12D$ to $1/6D$), while clusters of skewed cells are kept further from the wall;

- Hybrid GBL is judged to be a fine balance between accuracy and flexibility in grid generation, with the above due care and attention to detail. In particular, hybrid GBLs are nearly unescapable for real-world engineering applications with intricate geometries, e.g. with multiple obtuse or acute edges.

Analogous studies on grid quality effects are recommended for other paradigmatic high-Re flows in bluff body aerodynamics, such as the one around elon-

28

gated rectangular cylinders with separated and reattached boundary layer, and around real world structures, such as bridge decks and tall buildings. The relative significance of skewness viscosity with respect to other modelling approaches to turbulence such as wall resolved LES would be worth to be investigated as well.

Acknowledgments

References

Ahipo, Y., Traoré, P., 2009. A robust iterative scheme for finite volume discretization of diffusive flux on highly skewed meshes. Journal of Computational and Applied Mathematics 231, 478–491. doi:10.1016/j.cam.2009.03.015.

Antepara, O., Lehmkuhl, O., Borrell, R., Chiva, J., Oliva, A., 2015. Parallel adaptive mesh refinement for large-eddy simulations of turbulent flows. Computers and Fluids 110, 48–61. doi:10.1016/j.compfluid.2014.09.050.

Bearman, P.W., Obasaju, E.D., 1982. An experimental study of pressure fluctuations on fixed and oscillating square-section cylinders. Journal of Fluid Mechanics 119, 297–321. doi:10.1017/s0022112082001360.

Berrone, S., Marro, M., 2009. Space–time adaptive simulations for unsteady navier-stokes problems. Computers and Fluids 38, 1132–1144. doi:10.1016/j.compfluid.2008.11.004.

Blacker, T., Stephenson, M., 1991. Paving: A new approach to automated quadrilateral mesh generation. International Journal for Numerical Methods in Engineering 32, 811–847. doi:10.1002/nme.1620320410.

Bosch, G., Rodi, W., 1998. Simulation of vortex shedding past a square cylinder with different turbulence models. International Journal for Numerical Methods in Fluids 28, 601–616. doi:10.1002/(sici)1097-0363(19980930)28:4<601::aid-fld732>3.0.co;2-f.

Bruno, L., Coste, N., Fransos, D., 2012. Simulated flow around a rectangular 5:1 cylinder: Spanwise discretisation effects and emerging flow features. Journal of Wind Engineering and Industrial Aerodynamics 104-106. doi:10.1016/j.jweia.2012.03.018.

Bruno, L., Salvetti, M., Ricciardelli, F., 2014. Benchmark on the aerodynamics of a rectangular 5:1 cylinder: An overview after the first four years of activity. Journal of Wind Engineering and Industrial Aerodynamics 126. doi:10.1016/j.jweia.2014.01.005.

Bruno, L., Salvetti, M.V., 2017. Ufr 2-15, benchmark on the aerodynamics of a rectangular 5:1 cylinder (barc). URL: https://www.kbwiki.ercoftac.org/w/index.php/UFR_2-15_Description.

Cao, Y., Tamura, T., 2016. Large-eddy simulations of flow past a square cylinder using structured and unstructured grids. Computers and Fluids 137, 36–54. doi:10.1016/j.compfluid.2016.07.013.

Cao, Y., Tamura, T., 2017. Supercritical flows past a square cylinder with rounded corners. Physics of Fluids 29, 085110. doi:10.1063/1.4998739.

Cao, Y., Tamura, T., 2018. Aerodynamic characteristics of a rounded-corner square cylinder in shear flow at subcritical and supercritical reynolds numbers. Journal of Fluids and Structures 82, 473–491. doi:https://doi.org/10.1016/j.jfluidstructs.2018.07.012.

Cao, Y., Tamura, T., Kawai, H., 2020. Spanwise resolution requirements for the simulation of high-reynolds-number flows past a square cylinder. Computers & Fluids 196, 104320. doi:10.1016/j.compfluid.2019.104320.

Chen, Y., Djidjeli, K., Xie, Z.T., 2020. Large eddy simulation of flow past stationary and oscillating square cylinders. Journal of Fluids and Structures 97, 103107. doi:10.1016/j.jfluidstructs.2020.103107.

Deng, G., Piquet, J., Queutey, P., Visonneau, M., 1994. 2-d computations of unsteady flow past a square cylinder with the baldwin-lomax model. Journal of Fluids and Structures 8, 663–680. doi:10.1016/s0889-9746(94)90140-6.

Denner, F., van Wachem, B., 2014. Compressive vof method with skewness correction to capture sharp interfaces on arbitrary meshes. Journal of Computational Physics 279, 127–144. doi:10.1016/j.jcp.2014.09.002.

Denner, F., van Wachem, B., 2015. Tvd differencing on three-dimensional unstructured meshes with monotonicity-preserving correction of mesh skewness. Journal of Computational Physics 298, 466–479. doi:10.1016/j.jcp.2015.06.008.

Durao, D.F.G., Heitor, M.V., Pereira, J.C.F., 1988. Measurements of turbulent and periodic flows around a square cross-section cylinder. Experiments in Fluids 6, 298–304. doi:10.1007/bf00538820.

EN 1990, 2002. Eurocode - basis of structural design.

EN 1991-1-4, 2005. Eurocode 1: Actions on structures - part 1-4: General actions - wind actions.

Ferziger, J.H., 1993. Estimation and reduction of numerical error, in: Proceedings of the Symposium on Quantification of Uncertainty in Computational Fluid Dynamics, pp. 1–8.

Franke, R., Rodi, W., 1991. Calculation of vortex shedding past a square cylinder with various turbulence models, in: Eighth Symposium on 1urbu-

31

lent Shear Flows, Paper 20-1, Technical University of Munich, Germany. doi:10.1007/978-3-642-77674-8_14.

Haque, M., Katsuchi, H., Yamada, H., Nishio, M., 2016. Strategy to develop efficient grid system for flow analysis around two-dimensional bluff bodies. KSCE Journal of Civil Engineering 20, 1913–1924. doi:10.1007/s12205-015-0696-2.

Hoffman, J., 2005. Computation of mean drag for bluff body problems using adaptive dns/les. SIAM Journal on Scientific Computing 27, 184–207. doi:10.1137/040614463.

Issa, R.I., 1986. Solution of implicitly discretized fluid-flow equations by operator splitting. Journal of Computational Physics 62, 40–65. doi:10.1016/0021-9991(86)90099-9.

Jasak, H., 1996. Error Analysis and Estimation for the Finite Volume Method with Applications to Fluid Flows. Ph.D. thesis.

Juretić, F., Gosman, A.D., 2010. Error analysis of the finite-volume method with respect to mesh type. Numerical Heat Transfer, Part B: Fundamentals 57, 414–439. doi:10.1080/10407791003685155.

Kato, M., Launder, B.E., 1993. The modeling of turbulent flow around stationary and vibrating square cylinders, in: Ninth Symposium on Turbulent Shear Flows, Paper 10-4, Kyoto, Japan.

Ke, J., 2019. RANS and hybrid LES/RANS simulations of flow over a square cylinder. Advances in Aerodynamics 1. doi:10.1186/s42774-019-0012-9.

Khosla, P., Rubin, S., 1974. A diagonally dominant second-order accurate implicit scheme. Computers and Fluids 2, 207–209. doi:10.1016/0045-7930(74)90014-0.

Launder, B., Spalding, D., 1974. The numerical computation of turbulent flows. Computer Methods in Applied Mechanics and Engineering 3, 269–289. doi:10.1016/b978-0-08-030937-8.50016-7.

Lee, B.E., 1975. The effect of turbulence on the surface pressure field of a square prism. Journal of Fluid Mechanics 69, 263–282. doi:10.1017/s0022112075001437.

Lee, N., Lee, H., Baek, C., Lee, S., 2016. Aeroelastic analysis of bridge deck flutter with modified implicit coupling method. Journal of Wind Engineering and Industrial Aerodynamics 155, 11–22. doi:10.1016/j.jweia.2016.04.010.

Lee, S., 1997. Unsteady aerodynamic force prediction on a square cylinder using $k - \varepsilon$ turbulence models. Journal of Wind Engineering and Industrial Aerodynamics 67-68, 79–90. doi:10.1016/s0167-6105(97)00064-0.

Leonard, B., 1979. A stable and accurate convective modelling procedure based on quadratic upstream interpolation. Computer Methods in Applied Mechanics and Engineering 19, 59–98. doi:10.1016/0045-7825(79)90034-3.

Liu, M., Xiao, L., Yang, L., 2015. Experimental investigation of flow characteristics around four square-cylinder arrays at subcritical reynolds numbers. International Journal of Naval Architecture and Ocean Engineering 7, 906–919. doi:10.1515/ijnaoe-2015-0063.

Lyn, D.A., Einav, S., Rodi, W., Park, J.H., 1995. A laser-doppler velocimetry study of ensemble-averaged characteristics of the turbulent wake of a square cylinder. Journal of Fluid Mechanics 304, 285–319. doi:doi:10.1017/S0022112095004435.

Lyn, D.A., Rodi, W., 1994. The flapping shear layer formed by flow separation from the forward corner of a square cylinder. Journal of Fluid Mechanics 267, 353. doi:10.1017/s0022112094001217.

Mannini, C., Sbragi, G., Schewe, G., 2016. Analysis of self-excited forces for a box-girder bridge deck through unsteady rans simulations. Journal of Fluids and Structures 63, 57–76. doi:10.1016/j.jfluidstructs.2016.02.007.

Mannini, C., Šoda, A., Schewe, G., 2010. Unsteady rans modelling of flow past a rectangular cylinder: Investigation of reynolds number effects. Computers and Fluids doi:10.1016/j.compfluid.2010.05.014.

Mariotti, A., Salvetti, M.V., Omrani, P.S., Witteveen, J.A., 2016. Stochastic analysis of the impact of freestream conditions on the aerodynamics of a rectangular 5:1 cylinder. Computers and Fluids doi:10.1016/j.compfluid.2016.06.008.

Moore, D.M., Letchford, C.W., Amitay, M., 2019. Energetic scales in a bluff body shear layer. Journal of Fluid Mechanics doi:10.1017/jfm.2019.480.

Murakami, W., Mochida, A., 1995. On turbulent vortex shedding past 2d square cylinder predicted by cfd. Journal of Wind Engineering and Industrial Aerodynamics 54-55, 191–211. doi:10.1016/0167-6105(94)00043-D.

Muzaferija, S., 1994. Adaptative finite volume method for flow prediction using unstructured meshes and multigrid approach. Ph.D. thesis.

Nakane, I., 2013. Effectiveness of grid orthogonality on body fitted curvilinear coordinate system in cfd. International Journal of Environmental Science and Development 4. doi:10.7763/ijesd.2013.v4.329.

Nieto, F., Owen, J.S., Hargreaves, D.M., Hernandez, S., 2015. Bridge deck flutter derivatives: Efficient numerical evaluation exploiting their interdependence. Journal of Wind Engineering and Industrial Aerodynamics 136, 138–150. doi:10.1016/j.jweia.2014.11.006.

Nishimura, H., 2001. Fundamental study of bluff body aerodynamics (in Japanese). Ph.D. thesis.

Noda, H., Nakayama, A., 2003. Free-stream turbulence effects on the instantaneous pressure and forces on cylinders of rectangular cross section. Experiments in Fluids 34, 332–344. doi:10.1007/s00348-002-0562-0.

Oka, S., Ishihara, T., 2009. Numerical study of aerodynamic characteristics of a square prism in a uniform flow. Journal of Wind Engineering and Industrial Aerodynamics 97, 548–559. doi:10.1016/j.jweia.2009.08.006.

de Oliveira Samel Moraes, A., da Cunha Lage, P., Cunha, G., Silva, L., 2013. Analysis of the non-ortogonality correction of finite volume discretization on unstructured meshes,, in: 22nd International Congress of Mechanical Engineering (COBEM 2013).

Otsuki, Y., Fuji, K., Washizu, K., Ohya, A., 1978. Wind tunnel experiments on aerodynamic forces and pressure distributions of rectangular cylinders in a uniform flow, in: Proceedings of the Fifth Symposium on Wind Effects on Structures, pp. 169–176.

Pocha, J.J., 1971. On unsteady flow past cylinders of square cross-section. Ph.D. thesis.

Riberio, A.F.P., 2011. Unsteady rans modelling of flow past a rectangular 5:1 cylinder: investigation of edge sharpness effects. Proceedings of the Thirteenth International Conference on Wind Engineering, Amsterdam, The Netherlands .

Rocchio, B., Mariotti, A., Salvetti, M., 2020. Flow around a 5:1 rectangular cylinder: Effects of upstream-edge rounding. Journal of Wind Engineering & Industrial Aerodynamics 204, 104237. doi:10.1016/j.jweia.2020.104237.

Rodi, W., 1997. Comparison of les and rans calculations of the flow around bluff bodies. Journal of Wind Engineering and Industrial Aerodynamics 69-71, 55–75. doi:10.1016/s0167-6105(97)00147-5.

Rodi, W., 2004. Ufr 2-02, flow past cylinder. URL: https://www.kbwiki.ercoftac.org/w/index.php?title=UFR_2-02_Description.

Rodi, W., 2012. The ERCOFTAC knowledge base wiki - an aid for validating CFD models, in: Process and Plant Safety. Wiley-VCH Verlag GmbH & Co. KGaA, pp. 179–187. doi:10.1002/9783527645725.ch11.

Rodi, W., Ferziger, J.H., Breuer, M., Pourquié, M., 1997. Status of large-eddy simulation: Results of a workshop. Journal of Fluids Engineering 119, 248–262. doi:10.1115/1.2819128.

Sakamoto, H., Haniu, H., Kobayashi, Y., 1989. Fluctuating force acting on rectangular cylinders in uniform fow on rectangular cylinders with fully separated flow. Transactions of the Japan Society of Mechanical Engineers, Series B 55, 2310–2317.

Schewe, G., 2013. Reynolds-number-effects in flow around a rectangular cylinder with aspect ratio 1:5. Journal of Fluids and Structures 39, 15–26. doi:10.1016/j.jfluidstructs.2013.02.013.

Scruton, C., Rogers, E., Menzies, J., Scorer, R., 1971. Steady and unsteady wind loading of buildings and structures [and discussion]. Philosophical Transactions of the Royal Society of London Series A, Mathematical and Physical Sciences 269, 353–383. URL: https://www.jstor.org/stable/73873.

Shimada, K., Ishihara, T., 2002. Application of a modified $k-\varepsilon$ model to the prediction of aerodynamic characteristics of rectangular cross-section cylinders. Journal of Fluids and Structures 16, 465–485. doi:10.1006/jfls.2001.0433.

Shyy, W., Thakur, S., Wright, J., 1992. Second-order upwind and central difference schemes for recirculating flow computation. AIAA Journal 4, 923–932. doi:10.2514/3.11010.

Sohankar, A., Davidson, L., Norberg, C., 2000. Large eddy simulation of flow past a square cylinder: Comparison of different subgrid scale models. Journal of Fluids Engineering 122, 39–47. doi:10.1115/1.483224.

Tamura, T., Ito, Y., 1996. Aerodynamic characteristics and flow structures around a rectangular cylinder with a section of various depth/breadth ratios. Journal of Structural and Construction Engineering (Transactions of Architectural Institute of Japan) 486, 153–162. doi:10.3130/aijs.61.153_2.

Tamura, T., Miyagi, T., Kitagishi, T., 1998. Numerical prediction of unsteady pressures on a square cylinder with various corner shapes. Journal of Wind Engineering and Industrial Aerodynamics 74-76, 531–542. doi:10.1016/s0167-6105(98)00048-8.

Tang, H., Shum, K., Li, Y., 2019. Investigation of flutter performance of a twin-box bridge girder at large angles of attack. Journal of Wind Engineering and Industrial Aerodynamics 186, 192–203. doi:10.1016/j.jweia.2019.01.010.

Traoré, P., Ahipo, Y., Louste, C., 2009. A robust and efficient finite volume scheme for the discretization of diffusive flux on extremely skewed meshes in complex geometries. Journal of Computational Physics 228, 5148–5159. doi:10.1016/j.jcp.2009.04.007.

Trias, F.X., Gorobets, A., Oliva, A., 2015. Turbulent flow around a square cylinder at reynolds number 22000: a dns study. Computer and Fluids 123, 87–98. doi:10.1016/j.compfluid.2015.09.013.

Vickery, B., 1966. Fluctuating lift and drag on a long cylinder of square cross section in a smooth and turbulent flow. Journal of Fluid Mechanics 25, 481–494. doi:10.1017/S002211206600020X.

Wang, G., Vanka, S.P., 1997. Les of flow over a square cylinder, in: Chollet, J.P., Voke, P.R., Kleiser, L. (Eds.), Direct and Large-Eddy Simulation II, pp. 397–400. doi:10.1007/978-94-011-5624-0_37.

Wilkinson, R., 1974. On the vortex-induced loading on long bluff cylinders. Ph.D. thesis.

Yakhot, V., Orszag, S., Thangam, S., Gatski, T., Speziale, G., 1992. Development of turbulence models for shear flows by a double expansion technique. Physics of Fluids A4, 1510–1520. doi:10.1063/1.858424.

Younis, B.A., Przulj, V.P., 2005. Computation of turbulent vortex shedding. Computational Mechanics 37, 408–425. doi:10.1007/s00466-005-0713-2.

37

Yu, D., Kareem, A., 1996. Two dimensional simulation of flow around rectangular prisms. Journal of Wind Engeneering and Industrial Aerodynamics , 131–161doi:10.1016/s0167-6105(96)00076-1.

Zhang, Z., Xu, F., 2020. Spanwise length and mesh resolution effects on simulated flow around a 5:1 rectangular cylinder. Journal of Wind Engineering & Industrial Aerodynamics 202, 104186. doi:10.1016/j.jweia.2020.104186.

Zhu, G., Huang, S., Li, Q., 2020. Large-eddy simulation of the inflow turbulence transport and aerodynamics of a rectangular 5:1 cylinder with high-order numerical methods. Journal of Wind Engineering & Industrial Aerodynamics 207, 104366. doi:10.1016/j.jweia.2020.104366.